This paper describes objective technical results and analysis. Any subjective views or opinions that might be expressed in the paper do not necessarily represent the views of the U.S. Department of Energy or the United States Government.

SAND2024-01342J

Two-Well Injector Direct-phonon Terahertz Quantum Cascade Lasers

Nathalie Lander Gower[1], Shiran Levy[1], Silvia Piperno[1], Sadhvikas J. Addamane[2], John L. Reno[2], Asaf Albo[1, a)]

[1] Faculty of Engineering, Bar-Ilan University, Ramat Gan 5290002, Israel.

[2] Center for Integrated Nanotechnologies, Sandia National Laboratories, MS 1303, Albuquerque, New Mexico 87185-1303, USA.

a) asafalbo@gmail.com

Abstract

We present an experimental study on a Terahertz quantum cascade laser (THz QCL) design that combines both two-well injector and direct-phonon scattering schemes, i.e., a so-called two-well injector direct-phonon (TWI-DP) design. As a result of the two-well injector direct-phonon scheme presented here, the lasers benefit from both: a direct phonon scattering scheme for the lower laser level (LLL) depopulation and a setback for the doping profile that reduces the overlap of the doped region with the active laser states. Additionally, our design has also an efficient isolation of the active laser levels from excited and continuum states as indicated by negative differential resistance (NDR) behavior all the way up to room temperature. This scheme serves as a good platform for improving the temperature performance of THz QCLs as indicated by the encouraging temperature performance results of the device with a relatively high doping level of 7.56×10^{10} cm^{-2} and T_{max}~167 K. With the right optimization of the MBE growth and interfaces quality, the injection coupling strength, and the doping density and its profile, the device could potentially reach higher temperatures than the latest records reached for the maximum operating temperature (T_{max}) of THz QCLs.

Sandia National Laboratories U.S. DEPARTMENT OF ENERGY NNSA

This article has been authored by an employee of National Technology & Engineering Solutions of Sandia, LLC under Contract No. DE-NA0003525 with the U.S. Department of Energy (DOE). The employee owns all right, title and interest in and to the article and is solely responsible for its contents. The United States Government retains and the publisher, by accepting the article for publication, acknowledges that the United States Government retains a non-exclusive, paid-up, irrevocable, world-wide license to publish or reproduce the published form of this article or allow others to do so, for United States Government purposes. The DOE will provide public access to these results of federally sponsored research in accordance with the DOE Public Access Plan https://www.energy.gov/downloads/doe-public-access-plan.

Until today, the electromagnetic spectrum has been divided between electronic sources for long wavelengths (longer than ~0.3mm) and photonic devices for shorter wavelengths (shorter than ~0.03 mm). In the longer wavelength regime, electronic devices like frequency multipliers and transistors are the main sources [1]. The shorter wavelength regime can be attainable through photonic devices like semiconductor lasers and light emitting diodes [1]. However, between the infrared frequency range (approximately 10 THz- 430 THz) and microwave frequency range (approximately 10-300 GHz) there is a technological gap, called the "Terahertz (THz) gap" (approximately 300 GHz – 10 THz) [1], [2].

THz radiation has many applications, mainly because this radiation is nonionizing but can penetrate many materials such as skin, tissue, papers, fabrics, and plastics in a non-invasive way [3]. This, together with the fact that THz radiation provides a good contrast for imaging, makes this range of the spectrum particularly appealing for fields such as biomedicine [4], [5], security [6], astronomy [7], chemistry [8], and spectroscopy [9]-[11].

THz quantum cascade lasers (QCLs) are currently the most efficient THz source. In 2012, the maximum operating temperature (T_{max}) reached ~ 200 K [12]. Between 2012 and 2019, there was minimal progress in the temperature operation of THz QCLs. It was not until 2019 that a slight improvement was seen, with a T_{max} of ~ 210 K reported for a $GaAs/Al_{0.25}Ga_{0.75}As$ THz-QCL utilizing thermoelectric cooling (TEC) [13]. From 2019 there was a subsequent period of rapid advancement. In 2021, a portable device was launched, when a T_{max} of ~250 K was achieved and demonstrated [14]. Subsequently, in 2023, there was further progress, and the T_{max} reached ~261 K in a similar device by the same group [15]. These devices still required TEC and the temperature was reached in pulsed operation. Currently, similar T_{max} values were not reported by other groups,

indicating how big of a challenge this represents. Portable devices still remain unavailable for widespread use.

Consequently, despite the large number of potential applications, THz QCLs' applicability remains restricted due to the lack of portability. The main limitation arises from the requirement of either large cooling machinery, which hinders portability and compactness, or portable devices that utilize only TEC but fail to achieve reasonable output powers in the milliwatt range, making them still unsuitable for many practical applications. Hence, the prime goal in the field is to reach room temperature operation paired with a significant lasing output power. The physics and limitations behind the temperature performance of THz QCLs need to be better understood to keep improving the temperature performance of the devices.

Standard vertical-transition THz QCLs' temperature operation is mainly limited by the thermally activated longitudinal optical (LO) phonon scattering from the upper laser level (ULL) to the lower laser level (LLL) [16]. This limitation was overcome by designing highly diagonal structures, which significantly reduce thermally activated LO-phonon scattering [17], [18].

Thermally activated leakage into the continuum [18], mainly when using barriers with a low Al content (approximately 15% and lower), limits the temperature performance in highly diagonal THz QCLs structures. When aluminum content was increased to 30%, thermally activated leakage of charged carriers into excited bound states was still observed [19], [20] and proved to be harmful for the temperature performance. Pushing both excited and continuum states to higher energies to suppress these leakage paths was possible by combining high barriers with thin wells [19], [21], [22].

Clear negative differential resistance (NDR) behavior in the current voltage (I-V) curves was observed in carefully engineered devices all the way up to room temperature [19], [21], [22].

A clear NDR region means that all thermally activated leakage paths for electrons were suppressed, and the electron transport occurs only within the laser´s active subbands. This way, a clean n-level system was obtained, n being the number of the laser's active subbands [19], [21], [22]. A clean n-level system is thus a system where all electron transport occurs only within the active laser states and no significant leakages to the excited states and continuum are observed. Additionally, carrier populations in states other than the active laser states are negligible in clean n-level systems. Considering this, the strategy has been to design THz QCLs that have as close as possible to clean n-level systems, especially at high temperatures. This strategy of achieving a clean n-level system, led to the latest recorded T_{max} of ~250 K [14] and ~261 K [15] and this is the strategy used in our research as well.

The designs that reached the T_{max} of ~250 K [14] and ~261 K [15] are two-well (TW) designs supporting clean three-level systems, like a design demonstrated beforehand with small variations (Design HB2 in Ref. [21]). Likewise, there were other designs which proved to support a clean n-level system. Such is the case of a resonant-phonon design presented in 2016 [19], [23], a split-well direct-phonon (SWDP) proposed in 2019 [22], [24]–[25], and more recently a split-well resonant-phonon (SWRP) device presented and demonstrated in 2023 [26]-[28]. However, it is not clear why designs with very similar characteristics show very different T_{max} values, hence, the investigation is still ongoing.

Here, we suggest another design with clean n-level system. Our design is a two-well injector direct-phonon (TWI-DP) structure, which combines both two-well injector and direct-phonon scattering schemes. The direct-phonon scattering scheme is of high potential for demonstrating beyond state-of-the-art temperature performance of THz QCLs due to its several advantages compared to resonant-phonon structures. It has a very fast depopulation of the LLL

solely by LO-phonon scattering (no resonant tunneling is involved) and it is less sensitive to misalignment of the laser levels due to the Poisson effect [21], [22], [29]. However, the direct-phonon scheme also has one main disadvantage, namely, the large overlap of the doping profile with the active laser states, which results in enhanced gain broadening. This disadvantage is assumed to prevent significant improvements of the temperature performance of direct-phonon schemes [22], [30].

As a result of the two-well injector direct-phonon scheme presented here, the lasers benefit from a direct phonon scattering scheme for the rapid depopulation of the LLL, without the disadvantages of former direct-phonon designs. The added advantage in our design is the double injection scheme, that resulted in a setback for the doping profile and reduces the overlap of the doped region with the active laser states, minimizing this way the significant gain broadening present in previous designs. Additionally, just as the structures mentioned earlier, our design also has an efficient isolation of the active laser levels from excited and continuum states as indicated by NDR behavior up to room temperature [14], [19], [21], [22]. This results in THz QCLs with a direct-phonon scheme with a clean laser-level system and a setback for the doping profile.

As can be seen in Fig.1, the structure is based on four subbands in each module (all other levels are considered parasitic). As opposed to the TW designs mentioned before [14], [21], here the injection level is a doublet. The injection occurs through resonant tunnelling between the injection doublet and the ULL of the next module (levels 4, 5 and 6 in the scheme), the anticrossing value is 2.46 meV (Table 2). The LLL (level 3 in the scheme) and the injector doublet level of the following module (levels 1 and 2 in the scheme) are aligned to form a direct phonon scattering scheme similar to that of the TW scheme [14], [21], [31]–[33].

Here, we investigate a diagonal ($f \sim 0.55$) TWI-DP THz QCL with $Al_{0.3}Ga_{0.7}As$ barriers (Fig. 1). The doping level is ~9.11×10^{16} cm^{-3} - in the 83 Å quantum well, an integral value of ~7.56×10^{10} cm^{-2}. The wafer was grown by molecular beam epitaxy (MBE) and labelled VB0982. More details regarding the design, fabrication details, and device parameters can be found in Tables 1 and 2.

It can be seen in the energy scheme in Fig.1 that the active subbands (levels 1–4 in scheme) are well separated from excited states. The first relevant excited state above the ULL (level 11) is energetically located about ∼105 meV higher than the ULL (Table 2). Level 7 in the scheme is lower and closer to the ULL but there is little overlap between the two, as apart from the energy separation, they are separated by a potential barrier. The irrelevance of the lower laying level 7 is also verified by the NDR signature seen in the I-V curves all the way to room temperature, which indicate no significant thermally activated leakages.

A lasing frequency of ∼3.97 THz (lasing energy of ∼16.4 meV) was observed (Fig. 2 inset) with respect to the designed lasing value of ∼4.23 THz (lasing energy of ∼17.5 meV in Table 1). Pulsing conditions were 400 ns at 500 Hz, corresponding to a 0.02% duty cycle. This extremely low-duty cycle is typically necessary to avoid device heating and obtain maximum lasing temperatures. The device fabricated from the VB0982 wafer demonstrated a relatively high maximum operating temperature of $T_{max} \sim 167$ K (Fig. 2). While undertaking the measurements a signal was still observed at a temperature of ~171 K (not recorded). This temperature was reached with a relatively high doping density value of ~7.56×10^{10} cm^{-2} as stated before. Two different segments can be observed in the shape of the L-I curves up to 84 K. We attribute the change in the slope to the heating of the electrons with increasing current [34] and the high excess electron temperature at lower lattice temperatures [16], [35]. At higher temperatures the electrons cool down, as explained in the analysis of the output power plots below, and the slope is continuous.

In Fig. 3, the I-V curves show clear NDR behavior all the way up to room temperature, indicating a clean n-level system. The threshold current (J_{th}) vs. temperature curve is presented in Fig. 4(a). A relatively high characteristic temperature $T_0 \approx 326$ K is observed. For comparison, in the TW design of Ref. [14], where the scheme also supported a clean n-level system and lased at ~ 4 THz, T_0 was ≈260 K. J_{th} rises exponentially, an indication of the suppression of leakage to continuum [36], and its behavior can be well characterized by the standard model of $J_{th} = J_1 + J_0 e^{\frac{T}{T_0}}$. The high value of J_{th} at low temperatures is due to the high doping density in this structure.

To identify the physical mechanism limiting the temperature performance of our THz QCL design, we analyzed the light output power (P_{out}) vs temperature data (Fig. 4 (b)). The activation energy, (E_a), was extracted by the best fit to the data using Arrhenius plots using the formula $\ln(1 - \frac{P_{out}(\mathrm{T})}{P_{out}\,\mathrm{max}}) \approx \ln(a) - \frac{E_a}{KT}$, where a is a constant, as described in Ref. [16]. The activation energy extracted from Fig. 4(b) is ∼19 meV, a reasonable value (expected value from the measured optical transition was ∼18.5 meV, Table 1), indicating the thermally activated LO-phonon relaxation. The matching values of extracted and expected activation energies also imply the cooling of the electrons in the ULL to the lattice temperature. To extract a physical value that matches the expected value, we needed to apply our method in a range of temperatures where the electron temperature and the lattice temperature are equal. This value is obtained when ignoring the data for low temperatures, because of the presence of significant electron heating in this temperature range [16], [21], [22], [37]. As explained in previous works [16], [37], above a lattice temperature of ~100 K, the difference between the electron temperature in the ULL and the lattice temperature (the excess temperature) remains constant and in most devices the electrons cool down to the lattice temperature. Based on this, we can assume zero-excess temperature of the ULL for

lattice temperature values above ~100 K. According to the extracted activation energy value, we can establish that thermally activated leakage channels through excited states are sufficiently suppressed. The activation energy extracted matches the expected value calculated from the measured lasing frequency and supports our assumption that there is no excess electron temperature. Excess electron temperature can cause a change in the slope, resulting in an underestimation of the activation energy value which becomes not physical. As observed in the plot, at lower temperatures, a different result was observed from the analysis of the P_{out} data. The extracted activation energy value there was of ~ 4 meV. This value is not physical and is attributed to the high electronic temperature of the ULL in comparison to the lattice temperature in this temperature range [16], [37]. The different behaviors at low and high lattice temperatures (temperatures below and above ~100 K) can also be observed in the L-I curves, as explained above.

The dependence on temperature of the current dynamic range $\Delta J_d = (J_{max} - J_{th})$ was also analyzed, as the dynamic range is proportional to the output power and carries similar information. The dynamic range is reduced when the temperature increases, given that J_{th} increases and J_{max} decreases. The assumption here is that J_{th} approximates the nonlasing current J_{nl} (the current that will be measured on a nonlasing device at the same biasing conditions of J_{max}), thus $\Delta J_d = (J_{max} - J_{th}) \approx (J_{max} - J_{nl}) \propto P_{out}$. In Fig. 4b both P_{out} and the dynamic range are plotted as a function of temperature. As can be observed in Fig. 4b, the dynamic range curve remains in its initial slope (the slope at higher temperatures) for a larger range of temperatures, which allows us to prove the data obtained from the P_{out} analysis. This is because a fit of the current dynamic range data can be affected by underestimation of the electron excess temperature, as the electron temperature may increase at the nonlasing maximum current biasing conditions with respect to the threshold biasing conditions [37]–[40]. As done before for P_{out}, the best fit to the data using Arrhenius plots

according to $\ln\left(1-\frac{\Delta J_d(T)}{\Delta J_{d\,max}}\right) \approx \ln(b) - \frac{E_a}{kT}$ where b is a constant, was utilized to extract the activation energies for the current dynamic range. The extracted activation energy from ΔJ_d was ~20 meV (Fig. 4(b)), which also matches the expected value measured from the optical transition.

Both the transport and emission processes are influenced by the same dynamics, as indicated by the similar behavior of the temperature dependence of ΔJ_d and $P_{out}(T)$, especially close to T_{max}. Therefore, inter-module leakage does not contribute significantly to the current density.

In Fig. 5, J_{max} as a function of temperature is plotted all the way up to room temperature. This plot shows a very interesting behavior. As explained in previous works, J_{max} in clean *n*-level systems is a powerful tool that helps us understand the dynamics of the current [22], [30], [41]. We can treat our system as an effective three level system and describe it by the Kazarinov-Suris formula [22], [30], [41], [42]:

(1)

$$J = eN \times \frac{2\Omega^2 \tau_\parallel}{4\Omega^2 \tau \tau_\parallel + \omega_{21}^2 \tau_\parallel^2 + 1}$$

where Ω is the coupling between the injector and the ULL subbands across the barrier, τ is the ULL lifetime, $\tau_\parallel$ is the dephasing time between the ULL and the injector, and ω_{21} is the energy misalignment between the two. Two different regions can be derived from this equation as explained in previous works [22], [30], [37]. One is the strong coupling regime, when $\tau \gg \frac{1}{4\Omega^2 \tau_\parallel}$ [43], [44], and the other is the weak coupling regime where $\tau \ll \frac{1}{4\Omega^2 \tau_\parallel}$. The strong coupling regime can be divided in two subregions, i.e., lasing and non lasing subregions.

In Fig. 5 we can identify two different regions which both correspond to the strong coupling regime as explained before. Region 1 in the graph, is under lasing condition. Here $J_{max} \sim \frac{1}{\tau} \approx \frac{1}{\tau_{st}}$, meaning the transport is strongly limited by the ULL lifetime and the maximum current density decreases while the temperature increases [43].

Region 2 in the graph, represents the strong coupling regime under non-lasing condition. This region starts at around ~150 K. In this region, the dominant process is the non-radiative scattering rate, which increases as the temperature increases, $J_{max} \sim \frac{1}{\tau} \approx \frac{1}{\tau_{nr}}$, hence J_{max} will start to increase. There may be an optical signal measured after this temperature but, because of the transport being governed by the non-radiative lifetime as opposed to the stimulated emission rate, the signal is very low and disappears quickly. In Fig. 5, there is a significant raise of the J_{max}, this is because of the relatively high oscillator strength and lasing frequency of the device, which contribute to low τ_{nr} value and its fast drop with temperature increase. In our device this behavior continues up to room temperature.

The weak coupling regime, where the resonant tunneling is governed by dephasing since $J_{max} \sim \tau_{\parallel}$, is not observed in our device as opposed to former devices where this regime was clearly observed [22], [30], [37]. This is a good indication that the resonant tunneling is not affected even at high temperatures.

The main consideration when realizing this design was its potential improvement due to the reduced overlap between doped and active laser regions. Considering this, we think that further optimization and adjustment of the injection coupling, the oscillator strength, and doping density and its profile could potentially lead to better temperature performance. Enhancing the injection coupling in this design could prove to be particularly challenging considering the resonant

tunneling is between three levels (the two injectors and ULL) and through two barriers. This could be achieved by modifying the barriers' thicknesses.

Additionally, the quantity of carriers per module in this design is in the same order as other designs, hence, we do not think that the quantity of carriers should be the issue limiting the temperature operation. Nevertheless, studying the effect of the doping density, its profile and its spatial position is of utter importance and the right optimization could lead to potential enhancement in the temperature operation of the device.

Moreover, based on our current understanding, the main limitation relies on the MBE growth and interfaces' quality [45]. We assume that optimizing the quality of the interfaces [46] and MBE growth will lead to better temperature performance. Further optimization of the barriers, such as reducing the Al composition to 25%, could also reduce effects related to the interface roughness scattering.

In conclusion, we experimentally demonstrate a two-well-injector direct-phonon (TWI-DP) scheme for THz QCLs, which allows efficient isolation of these laser levels from excited and continuum states. Moreover, in our scheme there is a setback for the doping profile that reduces the overlap of the doped region with the active laser states. Also, in our structure, no increase in the dephasing of the resonant tunneling is observed when increasing the temperature, as opposed to structures studied before. Based on this, we do not think there is any physical limitation on this design, and with the right optimization of the MBE growth and interfaces' quality, the injection coupling strength, and the doping density and its profile, the device could potentially reach higher temperatures than the latest records reached for T_{max} of THz QCLs. These schemes serve as a good platform for improving the temperature performance of THz QCLs as indicated by the encouraging temperature performance results of the device with a relatively high doping level of 7.56×10^{10} cm^{-}

^{2} and T_{max}~167 K. Additionally, new encouraging results were obtained recently using this same scheme after some initial optimization, which led to a T_{max} of ~235 K [15].

Acknowledgments

The authors would like to acknowledge the Israel Science Foundation (ISF 1755/23) and the Israel Ministry of Science and Technology for their grants. The data of this research was taken at Massachusetts Institute of Technology (MIT). This work was performed, in part, at the Center for Integrated Nanotechnologies, an Office of Science User Facility operated for the U.S. Department of Energy (DOE) Office of Science. Sandia National Laboratories is a multimission laboratory managed and operated by National Technology & Engineering Solutions of Sandia, LLC, a wholly owned subsidiary of Honeywell International, Inc., for the U.S. DOE's National Nuclear Security Administration under contract DE-NA-0003525. The views expressed in the article do not necessarily represent the views of the U.S. DOE or the United States Government.

The data that support the findings of this study are available from the corresponding author upon reasonable request.

References

[1] B. S. Williams, ‘Terahertz quantum-cascade lasers’, Nat. Photonics, vol. 1, no. 9, pp. 517–525, Sep. 2007, doi: 10.1038/nphoton.2007.166.

[2] D. L. Woolard, R. Brown, M. Pepper, and M. Kemp, ‘Terahertz Frequency Sensing and Imaging: A Time of Reckoning Future Applications?’, Proc. IEEE, vol. 93, no. 10, pp. 1722–1743, 2005, doi: 10.1109/JPROC.2005.853539.

[3] R. J. Williams, ‘Frequency selective terahertz retroreflectors’, PhD Thesis, UMass Lowell, 2014.

[4] P. I. Abramov, E. V. Kuznetsov, L. A. Skvortsov, and M. I. Skvortsova, ‘Quantum-Cascade Lasers in Medicine and Biology (Review)’, *J. Appl. Spectrosc.*, vol. 86, no. 1, pp. 1–26, Mar. 2019, doi: 10.1007/s10812-019-00775-8.

[5] H. L. Hartnagel, V. P. Sirkeli, and P. Acedo, ‘THz Spectroscopy by Narrow Spectral Emission of Quantum Cascade Lasers for Medical Applications’, in *2021 International Semiconductor Conference (CAS)*, 2021, pp. 11–18. doi: 10.1109/CAS52836.2021.9604138.

[6] R. J. Grasso, ‘Defence and security applications of quantum cascade lasers’, in *Optical Sensing, Imaging, and Photon Counting: Nanostructured Devices and Applications 2016*, M. Razeghi, D. S. Temple, and G. J. Brown, Eds., SPIE, 2016, p. 99330F. doi: 10.1117/12.2238963.

[7] X. Lü, B. Röben, K. Biermann, *et al.*, ‘Terahertz quantum-cascade lasers for high-resolution absorption spectroscopy of atoms and ions in plasmas’, *Semicond. Sci. Technol.*, vol. 38, no. 3, p. 035003, Jan. 2023, doi: 10.1088/1361-6641/acb1cd.

[8] T. M. Korter and D. F. Plusquellic, ‘Continuous-wave terahertz spectroscopy of biotin: vibrational anharmonicity in the far-infrared’, *Chem. Phys. Lett.*, vol. 385, no. 1, pp. 45–51, 2004, doi: https://doi.org/10.1016/j.cplett.2003.12.060.

[9] S. Bartalini, L. Consolino, P. Cancio *et al.*, ‘Frequency-Comb-Assisted Terahertz Quantum Cascade Laser Spectroscopy’, *Phys Rev X*, vol. 4, no. 2, p. 021006, Apr. 2014, doi: 10.1103/PhysRevX.4.021006.

[10] M. Razeghi, Q. Lu, N. Bandyopadhyay *et al*., ‘Quantum cascade lasers: from tool to product’, Opt Express, vol. 23, no. 7, pp. 8462–8475, Apr. 2015, doi: 10.1364/OE.23.008462.

[11] M. S. Vitiello and P. De Natale, ‘Terahertz Quantum Cascade Lasers as Enabling Quantum Technology’, *Adv. Quantum Technol.*, vol. 5, no. 1, p. 2100082, 2022, doi: https://doi.org/10.1002/qute.202100082.

[12] S. Fathololoumi, E.B. Dupont, C.W.I. Chan *et al.,* ‘Terahertz quantum cascade lasers operating up to \sim 200 K with optimized oscillator strength and improved injection tunneling’, *Opt Express*, vol. 20, no. 4, pp. 3866–3876, Feb. 2012, doi: 10.1364/OE.20.003866.

[13] L. Bosco, M. Franckié, G. Scalari, M. Beck, A. Wacker, and J. Faist, ‘Thermoelectrically cooled THz quantum cascade laser operating up to 210 K’, *Appl. Phys. Lett.*, vol. 115, no. 1, p. 010601, 2019, doi: 10.1063/1.5110305.

[14] A. Khalatpour, A. K. Paulsen, C. Deimert, Z. R. Wasilewski, and Q. Hu, ‘High-power portable terahertz laser systems’, *Nat. Photonics*, vol. 15, no. 1, pp. 16–20, Jan. 2021, doi: 10.1038/s41566-020-00707-5.

[15] A. Khalatpour, M. C. Tam, S. J. Addamane, J. Reno, Z. Wasilewski, and Q. Hu, ‘Enhanced operating temperature in terahertz quantum cascade lasers based on direct phonon depopulation’, Appl. Phys. Lett., vol. 122, no. 16, p. 161101, Apr. 2023, doi: 10.1063/5.0144705.

[16] A. Albo and Q. Hu, ‘Investigating temperature degradation in THz quantum cascade lasers by examination of temperature dependence of output power’, *Appl. Phys. Lett.*, vol. 106, no. 13, p. 131108, 2015, doi: 10.1063/1.4916961.

[17] S. Kumar, Q. Hu, and J. L. Reno, ‘186 K operation of terahertz quantum-cascade lasers based on a diagonal design’, *Appl. Phys. Lett.*, vol. 94, no. 13, p. 131105, 2009, doi: 10.1063/1.3114418.

[18] A. Albo and Y. V. Flores, ‘Carrier Leakage Dynamics in Terahertz Quantum Cascade Lasers’, *IEEE J. Quantum Electron.*, vol. 53, no. 5, pp. 1–8, Oct. 2017, doi: 10.1109/JQE.2017.2740261.

[19] A. Albo, Q. Hu, and J. L. Reno, ‘Room temperature negative differential resistance in terahertz quantum cascade laser structures’, *Appl. Phys. Lett.*, vol. 109, no. 8, p. 081102, 2016, doi: 10.1063/1.4961617.

[20] D. Botez, S. Kumar, J. C. Shin, L. J. Mawst, I. Vurgaftman, and J. R. Meyer, ‘Temperature dependence of the key electro-optical characteristics for midinfrared emitting quantum cascade lasers’, *Appl. Phys. Lett.*, vol. 97, no. 7, p. 071101, 2010, doi: 10.1063/1.3478836.

[21] A. Albo, Y. V. Flores, Q. Hu, and J. L. Reno, ‘Two-well terahertz quantum cascade lasers with suppressed carrier leakage’, *Appl. Phys. Lett.*, vol. 111, no. 11, p. 111107, 2017, doi: 10.1063/1.4996567.

[22] A. Albo, Y. V. Flores, Q. Hu, and J. L. Reno, ‘Split-well direct-phonon terahertz quantum cascade lasers’, *Appl. Phys. Lett.*, vol. 114, no. 19, p. 191102, 2019, doi: 10.1063/1.5089854.

[23] C. W. I. Chan, A. Albo, Q. Hu, and J. L. Reno, ‘Tradeoffs between oscillator strength and lifetime in terahertz quantum cascade lasers’, *Appl. Phys. Lett.*, vol. 109, Nov. 2016, doi: 10.1063/1.4967244.

[24] N. Lander Gower, S. Piperno, and A. Albo, ‘Self-consistent gain calculations and carrier transport analysis for split-well direct-phonon terahertz quantum cascade lasers’, *AIP Adv.*, vol. 10, no. 11, p. 115319, 2020, doi: 10.1063/5.0015952.

[25] N. Lander Gower, S. Piperno, and A. Albo, ‘Comparison of THz-QCL Designs Supporting Clean N-Level Systems’, *Photonics*, vol. 8, no. 7, 2021, doi: 10.3390/photonics8070248.

[26] S. Levy, N. L. Gower, S. Piperno, S. J. Addamane, J. L. Reno, and A. Albo, ‘Split-well resonant-phonon terahertz quantum cascade laser’, Opt Express, vol. 31, no. 14, pp. 22274–22283, Jul. 2023, doi: 10.1364/OE.486446.

[27] S. Levy, N. L. Gower, S. Piperno, S. J. Addamane, J. L. Reno, and A. Albo, " Investigating the effect of doping concentration in split-well resonant-phonon terahertz quantum cascade laser structures," 2023, Opt. Letters (submitted).

[28] S. Levy, N. L. Gower, S. Piperno, S. J. Addamane, J. L. Reno, and A. Albo, “Analyzing the quantum transport on a split-well resonant-phonon terahertz quantum cascade laser within a self-consistent manner", 2023, (submitted).

[29] A. Albo and Y. V. Flores, ‘Temperature-Driven Enhancement of the Stimulated Emission Rate in Terahertz Quantum Cascade Lasers’, *IEEE J. Quantum Electron.*, vol. 53, no. 1, pp. 1–5, Feb. 2017, doi: 10.1109/JQE.2016.2631899.

[30] N. Lander Gower, S. Piperno, and A. Albo, ‘The Effect of Doping in Split-Well Direct-Phonon THz Quantum-Cascade Laser Structures’, *Photonics*, vol. 8, no. 6, 2021, doi: 10.3390/photonics8060195.

[31] S. Kumar, C. W. I. Chan, Q. Hu, and J. L. Reno, ‘Two-well terahertz quantum-cascade laser with direct intrawell-phonon depopulation’, *Appl. Phys. Lett.*, vol. 95, no. 14, p. 141110, 2009, doi: 10.1063/1.3243459.

[32] G. Scalari, M. I. Amanti, C. Walther, R. Terazzi, M. Beck, and J. Faist, ‘Broadband THz lasing from a photon-phonon quantum cascade structure’, *Opt Express*, vol. 18, no. 8, pp. 8043–8052, Apr. 2010, doi: 10.1364/OE.18.008043.

[33] B. S. Williams, S. Kumar, Q. Qin, Q. Hu, and J. L. Reno, ‘Terahertz quantum cascade lasers with double-resonant-phonon depopulation’, *Appl. Phys. Lett.*, vol. 88, no. 26, p. 261101, 2006, doi: 10.1063/1.2216112.

[34] M. S. Vitiello, G. Scamarcio, G. Scalari, J. Faist, C. Walther, and V. Spagnolo, ‘Hot electron effects and nanoscale heat transfer in Terahertz quantum cascade lasers’, in *Quantum Sensing and Nanophotonic Devices VI*, M. Razeghi, R. Sudharsanan, and G. J. Brown, Eds., SPIE, 2009, p. 722207. doi: 10.1117/12.814676.

[35] N. Lander Gower, S. Levy, S. Piperno, S. J. Addamane, J. L. Reno, and A. Albo, , 2023, “Extraction of the electron excess temperature in Terahertz Quantum Cascade Lasers from laser characteristics”, 2023,(submitted).

[36] A. Albo and Q. Hu, ‘Carrier leakage into the continuum in diagonal GaAs/Al0.15GaAs terahertz quantum cascade lasers’, *Appl. Phys. Lett.*, vol. 107, no. 24, p. 241101, 2015, doi: 10.1063/1.4937455.

[37] N. Lander Gower, S. Piperno, and A. Albo, ‘The Significance of Carrier Leakage for Stable Lasing in Split-Well Direct Phonon Terahertz Quantum Cascade Lasers’, *Photonics*, vol. 7, no. 3, 2020, doi: 10.3390/photonics7030059.

[38] M. S. Vitiello, G. Scamarcio,V. Spagnolo *et al.*, ‘Measurement of subband electronic temperatures and population inversion in THz quantum-cascade lasers’, *Appl. Phys. Lett.*, vol. 86, no. 11, p. 111115, 2005, doi: 10.1063/1.1886266.

[39] P. Harrison, D. Indjin, and R. W. Kelsall, ‘Electron temperature and mechanisms of hot carrier generation in quantum cascade lasers’, *J. Appl. Phys.*, vol. 92, no. 11, pp. 6921–6923, 2002, doi: 10.1063/1.1517747.

[40] V. Spagnolo, G. Scamarcio, H. Page, and C. Sirtori, 'Simultaneous measurement of the electronic and lattice temperatures in GaAs/Al0.45Ga0.55As quantum-cascade lasers: Influence on the optical performance', *Appl. Phys. Lett.*, vol. 84, no. 18, pp. 3690–3692, 2004, doi: 10.1063/1.1739518.

[41] N. L. Gower, S. Piperno, and A. Albo, 'The Response of Split-Well Direct-Phonon THz Quantum-Cascade Laser Structures to Changes in Doping', in *2022 47th International Conference on Infrared, Millimeter and Terahertz Waves (IRMMW-THz)*, 2022, pp. 1–2. doi: 10.1109/IRMMW-THz50927.2022.9895500.

[42] R. Kazarinov and R. A. Suris, 'Possible amplification of electromagnetic waves in a semiconductor with a superlattice', Sov. Physycs Semicond., vol. 5, pp. 707–709, Oct. 1971.

[43] I. Bhattacharya, C. W. I. Chan, and Q. Hu, 'Effects of stimulated emission on transport in terahertz quantum cascade lasers based on diagonal designs', *Appl. Phys. Lett.*, vol. 100, no. 1, p. 011108, 2012, doi: 10.1063/1.3675452.

[44] C. Sirtori, F. Capasso, J. Faist, A. L. Hutchinson, D. L. Sivco, and A. Y. Cho, 'Resonant tunneling in quantum cascade lasers', *IEEE J. Quantum Electron.*, vol. 34, no. 9, pp. 1722–1729, 1998, doi: 10.1109/3.709589.

[45] N. Lander Gower, S. Levy, S. Piperno, S. J. Addamane, J. L. Reno, and A. Albo, "Exploring the effects of molecular beam epitaxy growth characteristics on the temperature performance of two-well terahertz quantum cascade lasers", 2023 (submitted).

[46] Y. V. Flores and A. Albo, 'Impact of Interface Roughness Scattering on the Performance of GaAs/AlxGa1−xAs Terahertz Quantum Cascade Lasers', IEEE J. Quantum Electron., vol. 53, no. 3, pp. 1–8, 2017, doi: 10.1109/JQE.2017.2689743. Y. V. Flores and A. Albo, 'Erratum to "Impact of Interface Roughness Scattering on the Performance of GaAs/AlxGa1−xAs Terahertz Quantum Cascade Lasers" [Jun 17 Art. no. 2300208]', *IEEE J. Quantum Electron.*, vol. 53, no. 5, pp. 1–1, Oct. 2017, doi: 10.1109/JQE.2017.2732404.

Table 1: Main nominal design parameters and device data.

Device	Lasing Energy [meV]	E_{32} [meV]	Oscillator Strength	Nom. Expected Activation Energy [meV]	E_{5-11} [meV]	Layer Sequence [Å], barrier composition and doping level*	Process Details
Device VB0982	17.5	46.5	0.55	18.5	105	**34**/83/**32**/156/**20**/68 254 periods Total thickness 10 µm GaAs/**$Al_{0.3}Ga_{0.7}As$** 9.11×10^{16} cm^{-3} in the 83 Å wells (7.56×10^{10} cm^{-2}).	metal-metal (100 Å Ta / 2500 Å Au) Top contact n^+ layer was removed, bottom contact is 50 nm thick GaAs with doping of 5×10^{18} cm^{-3} Dry Etched Mesa size 150 µm × 1.4 mm

* The **AlGaAs** barriers in **bold** and the GaAs wells in roman, the doped layer in the sequence is underscored and the barriers' composition and doping details are elaborated in the following lines.

Table 2: Device parameters and performance.

Device (Wafer, Scheme)	**Injection coupling $\left(2\hbar\Omega_{ij}\right)$ [meV]**	**Design electric field [kV/cm]**	**τ^{0}_{ul} [ps]***	**τ^{0}_{21} [ps]****	**Lasing Energy [meV]**	**Lasing frequency [THz]**	**Expected Activation Energy [meV]**	**J_{th}(10 K) [A/cm2]**	**J_{th}(167 K) [A/cm2]**	**J_{max}(10 K) [A/cm^2]**	**Dynamic Range (10 K) [A/cm^2]**	**J_{max}(290 K) [A/cm^2]**	**T_{max} [K]**
Device VB0982	2.46	16.1	0.67	0.32	16.4	3.97	19.6	1379	1863	2029	650	1991	171

*ULL to LLL raw LO-phonon scattering time.

**LLL to Injector LO-phonon scattering time.

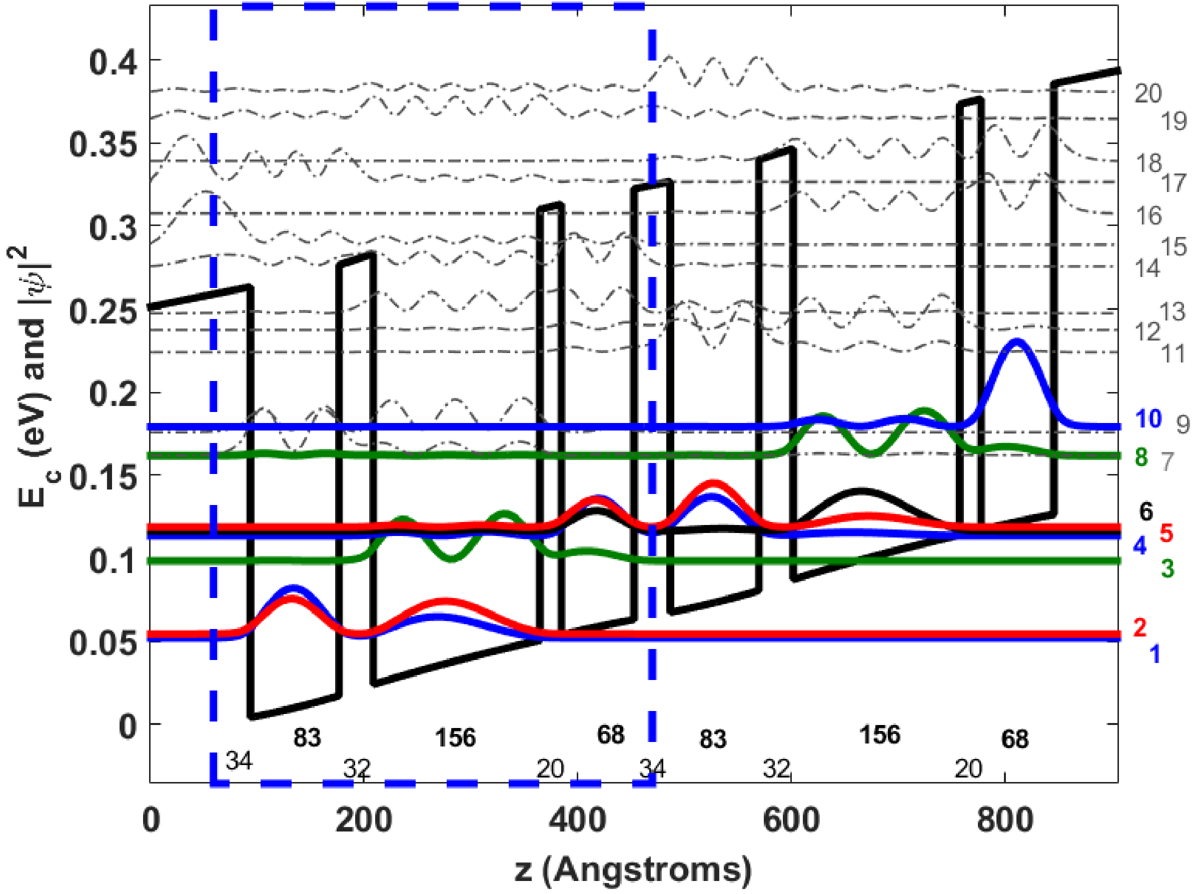

Figure 1: Band diagram of two sequential periods termed *module i* (left, marked by dashed-dotted box) and *module i+1* (right) of the two-well injector direct-phonon (TWI-DP) THz QCL structure with $Al_{0.3}Ga_{0.7}As$ barriers, corresponding to energy levels of Device VB0982 with doping level of ~7.56×10^{10} cm^{-2}. The 83 Å well layer is the doped layer. More details regarding the design and device parameters can be found in Table 1 and Table 2. Level 5 is the ULL, and level 3 is the LLL.

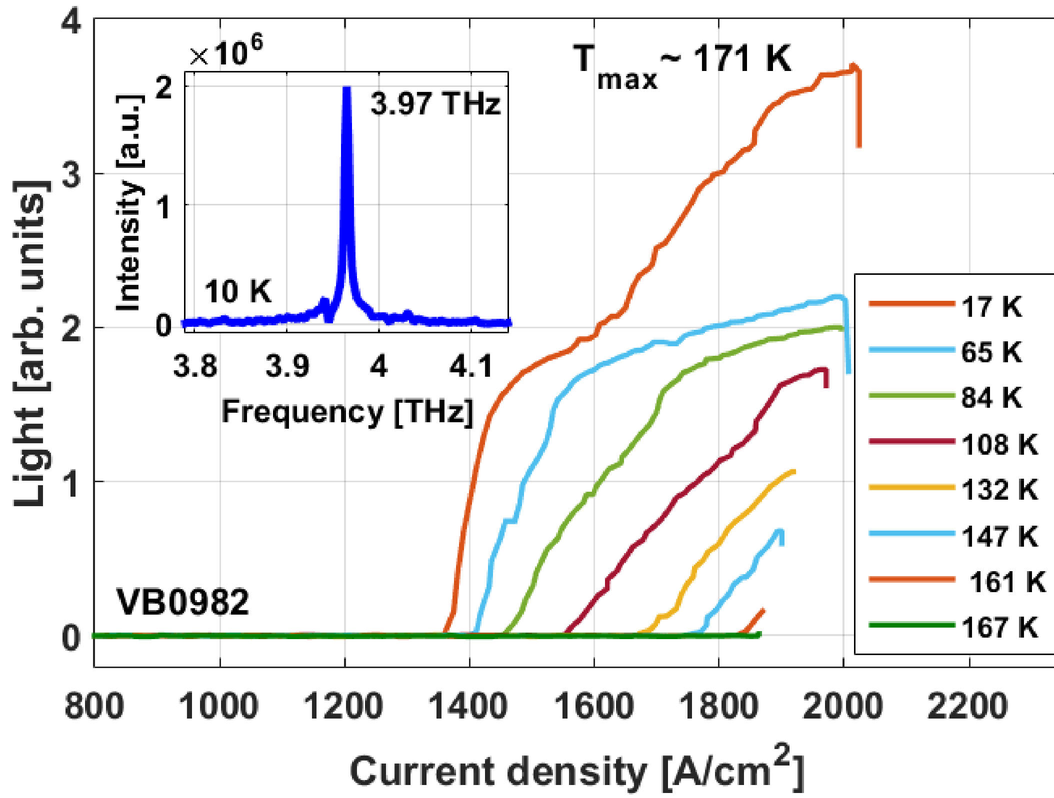

Figure 2: Pulsed light–current measurements of Device VB0982 with its lasing spectra as inset. More details on the structure can be found in Table 1, Table 2, and Figure 1. Pulsing conditions were 400 ns at 500 Hz, corresponding to a 0.02% duty cycle.

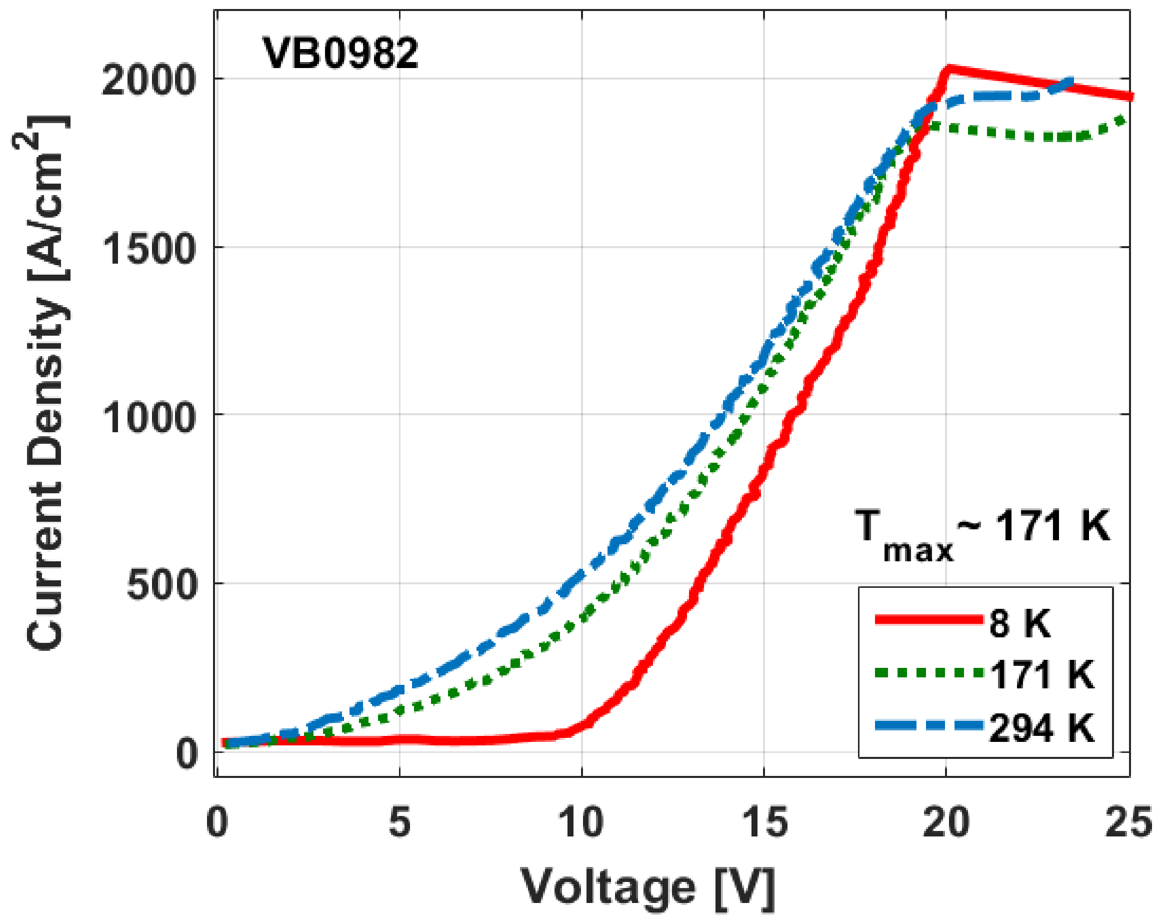

Figure 3: Current-voltage curves of Device VB0982 at low, around maximum operating, and room temperatures. Maximum operating temperature is indicated.

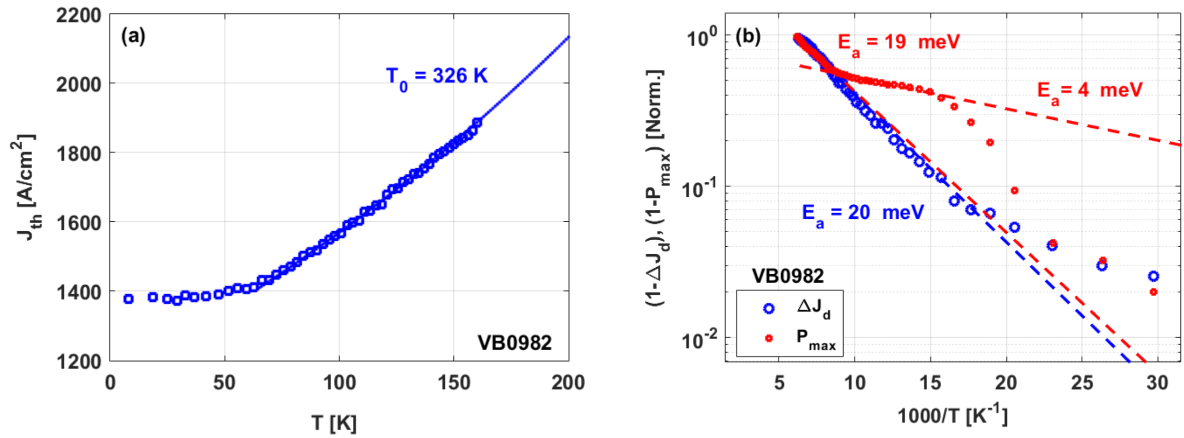

Figure 4: **(a)** Threshold current versus temperature of Device VB0982. **(b)** Activation energy that extracted from the laser's maximum output power (P_{max}) versus temperature data (red squares) and the current dynamic range $\Delta J_d = (J_{max}-J_{th})$ versus temperature data (blue circles), for Device VB0982.

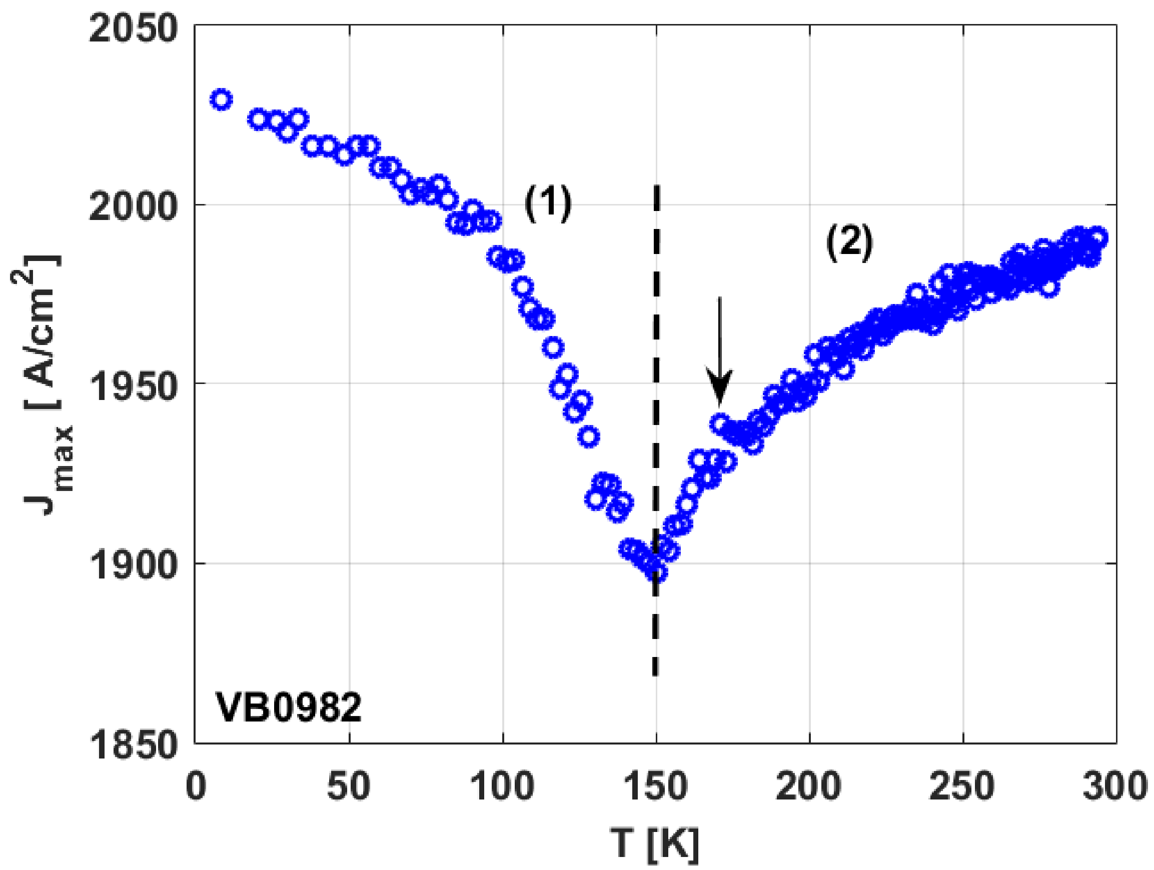

Figure 5: Maximum current densities versus temperature of Device VB0982 in blue circles. The two regions defined in the text and maximum operating temperature T_{max}, (black arrow) are marked.